of the Hg-supported LMs, either directly, by inducing the surface-parallel single- and double-layer phases, or indirectly, by imposing a high $\pi$-threshold on the standing-up phases and thus eliminating the low-$\pi$ standing-up phases observed in water-supported LMs. Hg-supported LMs, in which the film thickness and in-plane structure can be tuned in situ by varying the surface pressure, and in particular the phases revealed here, may prove more advantageous for studying nanosized electronic devices than the fixed-structure thiol self-assembled monolayers being used at present (*34*, *35*). They should provide new insight into the nature of the molecular-level interactions between organic and metallic molecules. Understanding such interactions is a central aim of two very important emerging fields: nanofabrication (*36*) and biometallic interfacing (*37–39*). They may also help to resolve fundamental controversies such as whether conformational disorder inhibits or promotes charge transfer across a monolayer in Hg-organics heterostructured devices (*40–42*). Our findings should hopefully lead to studies of LMs on additional subphases, further elucidating the subphase's important role in determining the LM's structure, and to studies of LMs of more complex systems on Hg subphases, such as fullerenes, nanotubes, and metallic nanoparticles, of much current interest to both basic and applied science.

**References and Notes**


1. V. M. Kaganer, H. Möhwald, P. Dutta, *Rev. Mod. Phys.* **71**, 779 (1999).
2. I. Kuzmenko *et al.*, *Chem. Rev.* **101**, 1659 (2001).
3. A. Pockels, *Nature* **43**, 437 (1891).
4. J. Jortner, M. Ratner, Eds., *Molecular Electronics* (Blackwell, Oxford, UK, 1997).
5. S. Grayer, Wolf *et al.*, *Nature* **328**, 63 (1987).
6. K. Kjaer, J. Als-Nielsen, C. A. Helm, L. A. Laxhuber, H. Möhwald, *Phys. Rev. Lett.* **58**, 2224 (1987).
7. P. Dutta, J. B. Peng, B. Lin, J. B. Ketterson, M. Prakash, *Phys. Rev. Lett.* **58**, 2228 (1987).
8. I. R. Peterson, G. Brezesinski, B. Struth, E. Scalas, *J. Phys. Chem. B* **102**, 9437 (1998).
9. T. Smith, *Adv. Colloid Interface Sci.* **3**, 161 (1972).
10. S. W. Barton, B. N. Thomas, E. B. Flom, F. Novak, S. A. Rice, *Langmuir* **4**, 233 (1988).
11. B. Harzallah, L. Bosio, R. Cortes, N. Errafii, *J. Chim. Phys. (France)* **93**, 1202 (1996).
12. O. M. Magnussen *et al.*, *Nature* **384**, 250 (1996).
13. R. C. Weast, M. J. Astle, W. H. Beyer, Eds., *Handbook of Chemistry and Physics* (CRC, Boca Raton, FL, ed. 66, 1986), pp. F174–F184.
14. M. Deutsch, B. M. Ocko, in *Encyclopedia of Applied Physics*, G. L. Trigg, Ed. (VCH, New York, 1998), vol. 23, p. 479.
15. J. Daillant, A. Gibaud, Eds., *X-Ray and Neutron Reflectivity: Principles and Applications* (Springer, Berlin, 1999).
16. J. Als-Nielsen *et al.*, *Phys. Rep.* **246**, 252 (1994).
17. J. Daillant, M. Alba, *Rep. Prog. Phys.* **63**, 1725 (2000).
18. G. L. Gaines, *Insoluble Monolayers at Liquid-Gas Interfaces* (Wiley, New York, 1966).
19. D. M. Small, *The Physical Chemistry of Lipids* (Plenum, New York, 1986).
20. O. M. Magnussen *et al.*, *Phys. Rev. Lett.* **74**, 4444 (1995).
21. The suprasurface "beach" observed there is replaced here by an equivalent subsurface depletion region (*26*).
22. E. Dimasi, H. Tostmann, B. M. Ocko, P. S. Pershan, M. Deutsch, *Phys. Rev. B* **58**, 13419 (1998).
23. X. Z. Wu, E. B. Sirota, S. K. Sinha, B. M. Ocko, M. Deutsch, *Phys. Rev. Lett.* **70**, 958 (1993).
24. A. Braslau *et al.*, *Phys. Rev. Lett.* **54**, 114 (1985).
25. C. Fradin *et al.*, *Nature* **403**, 871 (2000).
26. The tilts derived from the x-ray reflectivity have measurement and fit uncertainties of ~4° to 5°.
27. B. Lin, M. C. Shih, T. M. Bohanon, G. E. Ice, P. Dutta, *Phys. Rev. Lett.* **65**, 191 (1990).
28. G. A. Overbeck, D. Möbius, *J. Phys. Chem.* **97**, 7999 (1993).
29. V. M. Kaganer, E. B. Loginov, *Phys. Rev. Lett.* **71**, 2599 (1993).
30. M. Popescu, T. Gutberlet, M. Kastowsky, P. J. Koch, H. Bradaczek, *Thin Solid Films* **304**, 323 (1997).
31. S. Hazra, A. Gibaud, A. Desert, V. Gacem, N. Cowlam, *Physica B* **283**, 45 (2000).
32. P. Ganguly, D. V. Paranjape, S. K. Chaudhari, *J. Phys. Chem.* **97**, 11965 (1993).
33. M. Deutsch, O. M. Magnussen, B. M. Ocko, M. J. Regan, P. S. Pershan, in *Thin Films: Self-Assembled Monolayers of Thiols*, A. Ulman, Ed. (Academic Press, San Diego, CA, 1998), pp. 179–203.
34. M. A. Rampi, O. J. A. Schueller, G. M. Whitesides, *Appl. Phys. Lett.* **72**, 1781 (1998).
35. K. Slowinski, H. K. Y. Fong, M. Majda, *J. Am. Chem. Soc.* **121**, 7257 (1999).
36. A. Hatzor, P. S. Weiss, *Science* **291**, 1119 (2001).
37. B. Kasemo, *Surf. Sci.* **500**, 656 (2002).
38. E. Braun, Y. Eichen, U. Sivan, G. Bar-Yoseph, *Nature* **391**, 775 (1998).
39. Y. Maeda, H. Tabata, T. Kawai, *Appl. Phys. Lett.* **79**, 1181 (2001).
40. C. Boulas, J.V. Davidovits, F. Rondelez, D. Vuillaume, *Phys. Rev. Lett.* **76**, 4797 (1996).
41. A. Haran, D. H. Waldeck, R. Naaman, E. Moons, D. Cahen, *Science* **263**, 948 (1994).
42. K. Slowinski, M. Majda, *J. Electroanal. Chem.* **491**, 139 (2000).


43. Support to P.S.P. by the U.S. Department of Energy (grant DE-FG02-88-ER45379) and the National Science Foundation (grant DMR-01-124936) and to M.D. by the United States–Israel Binational Science Foundation, Jerusalem, is gratefully acknowledged. We thank D. Vaknin (Ames) for generous advice and drawings of the trough, and Y. Rabin and I. Kanter for a critical reading of the manuscript. Brookhaven National Laboratory is supported by the U.S. Department of Energy (contract DE-AC02-98CH10886).

11 September 2002; accepted 16 October 2002


# Simulation of Subduction Zone Seismicity by Dehydration of Serpentine

**David P. Dobson,[1,2]* Philip G. Meredith,[2] Stephen A. Boon[2]**

**We measured acoustic emission energy during antigorite dehydration in a multianvil press from 1.5 to 8.5 gigapascals and 300° to 900°C. There was a strong acoustic emission signal on dehydration, and analysis of recovered samples revealed brittle deformation features associated with high pore-fluid pressures. These results demonstrate that intermediate depth (50 to 200 kilometers) seismicity can be generated by dehydration reactions in the subducting slab.**

The origin of intermediate- and deep- (50 to 600 km) focus earthquakes within subducting oceanic slabs remains enigmatic. At these depths, rocks should deform by plastic flow rather than by the sudden brittle deformation that is prevalent in the shallow crust. Subducting oceanic lithosphere undergoes changes in mineralogy with increasing pressure and temperature, and these reactions have been invoked to explain deep earthquakes (*1–4*). Dehydration of the subducting slab and migration of fluids generates magma below back-arcs (*5*, *6*), but it is currently unclear whether these phase transformations can generate seismicity under the pressure-temperature (*P-T*) conditions of the subducting slab.

We performed acoustic emission (AE) studies of antigorite dehydration between 1.5 and 8.5 GPa under conditions pertinent to subduction. AEs are high-frequency elastic waves produced by rapid strain in solids and are analogous to seismic waves within Earth. Antigorite is the major hydrous phase in serpentinized peridotites and can be used as a proxy for hydrous phases in the slab. AE signals just above the dehydration temperature demonstrate that elastic strain waves associated with rapid deformation are a characteristic feature of dehydration under these conditions.

Experiments were performed in a 1000-metric-ton split-cylinder multianvil press (*7*). Cylinders 3 mm in diameter and 4 mm in length were cored from a natural Erzgebirge garnet serpentinite, and garnet-free cores were chosen as samples. These consisted of 90 to 95% antigorite $[Mg_{41.6}Fe^{2+}_{1.22}Al_{0.34}Fe^{3+}_{3.17}Si_{34}O_{85}(OH)_{62}]$ with minor chromium-diopside, olivine, and oxides. Samples were placed centrally in a stepped $LaCrO_3$ furnace in the high-pressure cell. Acoustic waveguides were placed between the sample and the anvils. We used either polycrystalline corundum or iron waveguides. Corundum has a low attenuation, maximizing the observed AE signal, but gen-

[1]Bayerisches Geoinstitut, Universität Bayreuth, D-95440 Bayreuth, Germany. [2]Department of Earth Sciences, University College London WC1E 6BT, UK.

*To whom correspondence should be addressed. E-mail: d.dobson@ucl.ac.uk

erates a large deviatoric stress on the sample. Iron waveguides maintain a low oxygen fugacity near the sample and ensure that AE signals are not due to brittle failure of the waveguides. The two anvils that contacted the waveguides had AE transducers mounted directly on their back truncations. Samples were compressed at room temperature and annealed at pressure and 350°C for 1 hour. They were then heated at a constant rate of 5°C/min to a maximum of 900°C. The dual-transducer arrangement allowed linear location of the source AE from the time difference between arrivals at each transducer $\Delta t$ from an AE event.

We observed AE events 100° to 150°C above the equilibrium dehydration temperature (*8–10*) (Fig. 1A). This overstep is due to the relatively fast heating rates in our experiments as compared to the equilibrium studies. Despite the metastable overstep, the AEs followed the form of the phase boundary. Two separate types of AE were observed. At pressures below 6.5 GPa, corresponding to the reaction $Mg_{48}Si_{34}O_{85}(OH)_{62}$ (antigorite) = 14 $Mg_2SiO_4$ (olivine) + 20 $MgSiO_3$ (enstatite) + 31 $H_2O$ (fluid), AEs were confined to very narrow temperature intervals. Above 6.5 GPa, AEs occurred across a wide temperature interval of 50°C or more. This pressure range corresponds to the reaction 5 $Mg_{48}Si_{34}O_{85}(OH)_{62}$ (antigorite) = 14 $Mg_7Si_2O_8(OH)_6$ (phase A) + 142 $MgSiO_3$ (enstatite) + 113 $H_2O$ (fluid). Below 6.5 GPa, the dehydration-related AEs consisted of either a single high-energy event at very low $\Delta t$ within the sample (Fig. 1B), or a small sample event immediately followed by a large event at $\Delta t$ within the waveguides (Fig. 1C). High-energy events were characterized by long durations and amplitudes not significantly higher than those of smaller events. This type of slow, medium-amplitude event is typical of propagation along a failure surface, with multiple overlapping small events that cannot be individually resolved.

We quenched samples from repeat experiments immediately after the large AE. The sample in Fig. 2A contains typical dehydration embrittlement features: oxide bands show displacements of up to 3 μm along a planar surface. The angular relationship between the plane and the direction of maximum compressive stress, $\sigma_1$, is typical of faults in the brittle regime, and the plane is decorated with dehydration products. Similar features have been observed in previous serpentine dehydration studies (*11*), but our experiments used realistic slab *P-T* conditions. Faulting was not observed in samples recovered from 8 GPa, where dehydration products were dispersed throughout the sample.

Recovered cells showed fractures within the waveguides (Fig. 2B) as well as sample hydraulic embrittlement. There was considerable recrystallization of the corundum wall material within the fractured waveguide. $MgO\text{-}SiO_2\text{-}Al_2O_3$ precipitates were sometimes observed within this recrystallized zone. The sample was the only source of silicate in the cell, and we consider precipitates within fractured waveguides, as well as the degree of recrystallization of fracture walls, to be evidence of open conduits to fluid flow during sample dehydration. These features probably formed by hydrofracture during dehydration, which is consistent with their orientation with respect to $\sigma_1$.

We observed three distinct forms of brittle failure associated with dehydration in our experiments. Below 6.5 GPa, the sample

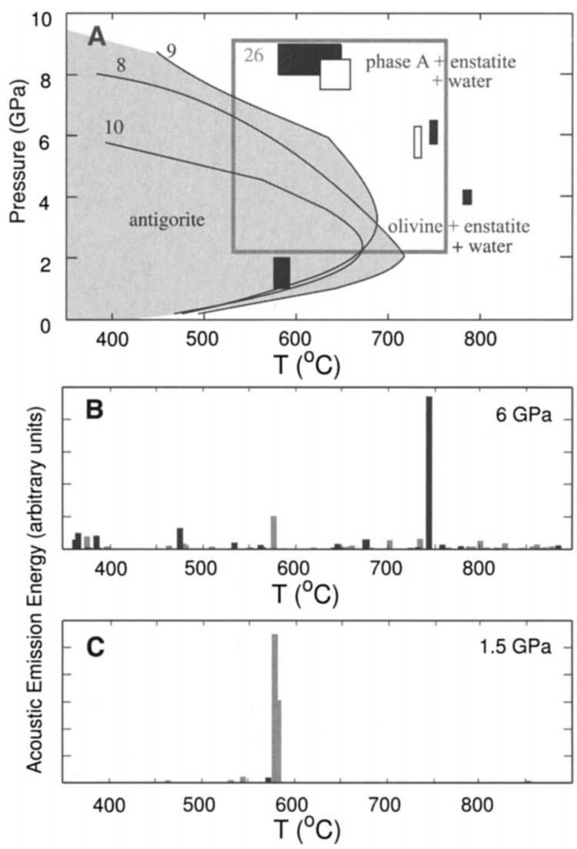


**Fig. 1.** AEs during antigorite dehydration. (**A**) *P-T* phase diagram (*8–10*) and observed AEs (small boxes): iron and corundum waveguides are indicated by open and solid boxes, respectively. The height of the boxes gives the pressure uncertainty. The large gray box indicates the range of observed AEs from (*26*). (**B** and **C**) Plots of AE energy versus temperature for experiments at (B) 6 and (C) 1.5 GPa, with corundum waveguides. Black symbols represent arrivals at $\Delta t < 0.5$ μs and gray symbols represent arrivals at $0.5\ \mu s < \Delta t < 2.5\ \mu s$. The low $\Delta t$ arrivals correspond to events that originated within the sample and the higher $\Delta t$ arrivals correspond to waveguide events. The large dehydration AEs are always initiated by an event within the sample.

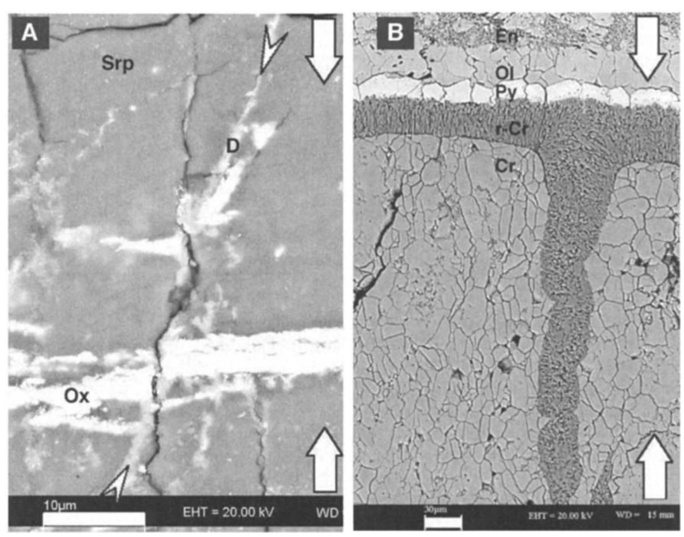


**Fig. 2.** Backscattered electron images of recovered samples; $\sigma_1$ is vertical in both images. (**A**) A sample recovered from 6 GPa and quenched after the large AE. The antigorite groundmass (Srp) has been faulted along the plane indicated by the arrowheads. The sense of the fault is dextral, with a 3-μm displacement, as indicated by the oxide bands (Ox). The light material (D) decorating the fault consists of a fine-grained mixture of antigorite dehydration products. (**B**) Recrystallized fracture in a corundum waveguide. The sample is at the top of the image, showing the olivine-pyrope reaction zone. The region of the waveguide in contact with the sample and within the fracture has completely recrystallized, indicating considerable fluid flux within the fracture. En, enstatite; Ol, olivine; Py, pyrope; Cr, corundum; r-Cr, recrystallized corundum.

failed by hydraulic embrittlement as increased pore pressure from dehydration reduced the effective normal stress sufficiently to bring the system into the brittle regime. Additionally, brittle components surrounding the sample failed by hydrofracture. Once an open conduit was established for draining the sample, significant AEs should cease, which would be consistent with a single large event. These mechanisms require a positive volume change of dehydration; otherwise, elevated pore pressures will not occur. Above 6.5 GPa, the antigorite dehydration reaction had a negative Clapeyron slope and volume change of reaction. In this case, hydraulic failure would not occur and we interpret the observed AE to be caused by collapse of the pressure medium around the reduced sample volume. This is consistent with a prolonged series of AEs as the reaction progresses.

Consider a subduction zone with a convergence rate of 10 mm/year and dehydration at 100 km depth and 600°C. The average heating rate for this slab is $10^{-10}$°C/min as compared to 5°C/min for the experiments. Given this difference of 10 orders of magnitude, can the natural system drain without fracturing? Let us assume that the main requirement to avoid brittle failure is to remove fluid from serpentine bodies, within the slab in the natural instance or from the laboratory sample. In addition to hydraulic failure, this can occur by diffusion, porous flow, or solution precipitation.

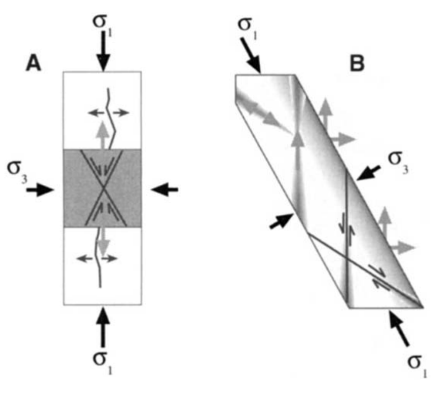


**Fig. 3.** Conceptual model of **(A)** the experimental geometry and **(B)** the subducting slab. The gray regions represent hydrated material and gray arrows indicate the direction of fluid draining. Black lines and arrows represent the mode of brittle failure in different regions. Experiments fail by hydraulic embrittlement within the sample and by hydrofracture in the waveguides. Hydrated regions in the slab lie along an upper zone and within preexisting faults deep within the slab. Failure in the upper and lower planes of hydrated slab occurs by hydraulic embrittlement, but subsequent draining of the products results in remobilization of the preexisting faults and further seismicity in the lower plane. $\sigma_1$ and $\sigma_3$ are the directions of maximum and minimum compressive stress, respectively.

Diffusive processes have a time dependence on distance squared. Thus, for our subduction scenario, the laboratory data would be appropriate to a serpentine body 700 m thick. In this scenario, larger bodies would be more likely to drain by hydraulic failure than in the experimental system. This thickness is similar to that of serpentenized zones in ophiolites. Furthermore, features in alpine ophiolites suggest that subducting oceanic lithosphere can be fractured by dehydration of serpentine bodies as thin as 1 m (*12*).

For porous draining, the maximum thickness of dehydrating material that will not cause hydraulic failure is related to the change in porosity during dehydration, the density difference between fluid and rock, and the permeability of the surroundings (*13*). It is difficult to estimate the permeability of the mantle. However, a 5- to 500-m-thick serpentinite body dehydrating under the above scenario would require an unrealistically high mantle permeability ($10^{-18}$ to $10^{-20}$), more typical of crystalline rocks in the upper crust (*14*), in order for hydraulic failure not to occur.

Solution precipitation can cause fluid inclusions to migrate up thermal gradients (*15*). Using the model from (*15*), the maximum migration velocities at 400° to 600°C are 0.3 to 10 m per million years, for a generous slab thermal gradient of 80 K/km at 120 km depth (*16*). In the same period, the slab will have advanced by 10 km. Taking a mean thermal migration velocity, and assuming that serpentine dehydration occurs within the top 200 km, the maximum thickness of serpentine body that can be drained by solution precipitation is 100 m. The temperature dependence of migration velocity implies that hydraulic failure will initiate within the cold slab, whereas draining by solution precipitation is possible in the surrounding mantle.

Focal mechanism solutions imply that intermediate-depth earthquakes are double-couple events without volume collapse or hydrofracture components. Serpentine dehydration can therefore only cause earthquakes shallower than 200 km (<6.5 GPa). However, other dehydration reactions may be viable at greater depths (*17*). Conceptual models for experimental and slab geometries are illustrated in Fig. 3. The experimental geometry (Fig. 3A) is a sandwich of hydrated sample between anhydrous waveguides, oriented along $\sigma_1$. In this case, hydraulic embrittlement occurs within the sample, which triggers fluid release into and hydrofracturing of the waveguides. The slab model (Fig. 3B) is considerably different. The upper several kilometers of oceanic crust are strongly hydrated by hydrothermal activity at mid-ocean ridges. In addition, the lower oceanic lithosphere may be hydrated along outer rise faults, to depths of several tens of kilometers, and dehydration along these old fault zones has been proposed as the source of lower plane earthquakes (*18*, *19*). The resulting slab model is one with a pervasively hydrated upper zone and sporadic hydration along old faults below this (Fig. 3B). At intermediate depths, the maximum compressive stress is often slab-parallel. Dehydration in the upper zone will result in hydraulic embrittlement and double-couple events consistent with upper plane seismicity (*20*). Deep slab regions will suffer hydraulic embrittlement of dehydrating regions. The released fluid will be drained from the slab in a process analogous to the experimental hydrofracture. In this scenario, however, dehydration occurs within a preexisting fault zone, and draining of high-pressure fluid along this zone of weakness will reduce the effective normal stress across the fault, allowing further thrust failure consistent with focal mechanism and body wave constraints (*21*, *22*).

We observe experimentally that serpentine dehydration results in low-energy events within the hydrous material but triggers large events in the stronger surroundings. We propose a similar hydraulic triggering process within the lower plane of double seismic zones, with dehydration embrittlement being responsible for upper plane seismicity. Low-amplitude tremors have recently been observed associated with large earthquakes at intermediate depths below the southwest Japanese subduction zone (*23*). We suggest that precursor tremors correspond to our experimentally observed dehydration triggering. Additionally, similar tremors are observed associated with magma flow in conduits, and intermediate-depth tremors after large earthquakes (*23*) might represent fluid draining similar to that which produced the recrystallization of the waveguides, post-AE, in our experimental system.

### References and Notes

1. C. Frohlich, *Annu. Rev. Earth Planet. Sci.* **17**, 227 (1989).
2. C. B. Raleigh, M. S. Patterson, *J. Geophys. Res.* **70**, 3965 (1965).
3. S. H. Kirby, W. B. Durham, L. A. Stern, *Science* **252**, 216 (1991).
4. H. W. Green, T. E. Young, D. Walker, C. H. Scholz, *Nature* **348**, 720 (1990).
5. I. Kushiro, *J. Geophys. Res.* **95**, 15929 (1990).
6. E. Bonatti, P. J. Michael, *Earth Planet. Sci. Lett.* **91**, 297 (1989).
7. N. Kawai, S. Endo, *Rev. Sci. Instrum.* **41**, 1178 (1970).
8. P. Ulmer, V. Trommsdorff, *Science* **268**, 858 (1995).
9. K. Bose, K. Navrotsky, *J. Geophys. Res.* **103**, 9713 (1998).
10. B. Wunder, W. Schreyer, *Lithos* **41**, 213 (1997).
11. E. H. Rutter, K. H. Brodie, *J. Geophys. Res.* **93**, 4907 (1988).
12. E. H. Hoogerduijn, R. L. M. Vissers, *Tectonophysics* **200**, 187 (1991).
13. T.-F. Wong, S.-C. Ko, D. L. Olgaard, *J. Geophys. Res.* **102**, 841 (1997).
14. W. F. Brace, *Int. J. Rock Mech. Min. Sci.* **17**, 241 (1980).
15. E. B. Watson, D. A. Wark, *Contrib. Mineral. Petrol.* **130**, 66 (1997).

16. J. H. Davies, D. J. Stevenson, *J. Geophys. Res.* **97**, 2037 (1992).
17. Hydrated basalt contains amphiboles and chlorite, which also fail by dehydration embrittlement (*23–25*).
18. T. Seno, Y. Yamanaka, *Geophys. Monogr. Am. Geophys. Union* 96 (American Geophysical Union, Washington, DC, 1996), pp. 347–355.
19. S. M. Peacock, *Geology* **29**, 299 (2000).
20. S. H. Kirby, E. R. Engdahl, R. Denlinger, *Geophys. Monogr. Am. Geophys. Union* 96 (American Geophysical Union, Washington, DC, 1996), pp. 195–214.
21. W. Jiao, P. G. Silver, Y. Fei, C. T. Prewitt, *J. Geophys. Res.* **105**, 28125 (2000).
22. R. Tibi, G. Bock, C. H. Estabrook, *J. Geophys. Res.* **107**, ESE1-1 (2002).
23. K. Obara, *Science* **296**, 1679 (2002).
24. B. R. Hacker, J. M. Christie, *Geophys. Monogr. Am. Geophys. Union* 56 (American Geophysical Union, Washington, DC, 1990), pp. 127–147.
25. S. A. F. Murrel, I. A. H. Ismail, *Tectonophysics* **31**, 207 (1976).
26. C. Meade, R. Jeanloz, *Science* **252**, 68 (1991).
27. D.P.D. is grateful for his Alexander von Humboldt Fellowship. Experiments were performed at the Bayerisches Geoinstitut under the EU "IHP to Research Infrastructures" Programme (contract no. HPRI-1999-CT-004 to D. C. Rubie).

19 August 2002; accepted 7 October 2002

# The Cause of Decreased Pan Evaporation over the Past 50 Years

**Michael L. Roderick and Graham D. Farquhar***

**Changes in the global water cycle can cause major environmental and socioeconomic impacts. As the average global temperature increases, it is generally expected that the air will become drier and that evaporation from terrestrial water bodies will increase. Paradoxically, terrestrial observations over the past 50 years show the reverse. Here, we show that the decrease in evaporation is consistent with what one would expect from the observed large and widespread decreases in sunlight resulting from increasing cloud coverage and aerosol concentration.**

It is now well established that the surface of Earth has, on average, warmed ~0.15°C decade$^{-1}$ over the past 50 years (*1*). One expected consequence of this warming is that the air near the surface should be drier, which should result in an increase in the rate of evaporation from terrestrial open water bodies. However, despite the observed increases in average temperature, observations from the Northern Hemisphere show that the rate of evaporation from open pans of water has been steadily decreasing over the past 50 years (*2*). This trend is general (*3*, *4*) but not universal (*5*). The contrast between expectation and observation is called the pan evaporation paradox. It is important to understand why pan evaporation has decreased despite the increases in average temperature in order to make more robust predictions about future changes in the hydrological cycle.

Two proposals for the decline in pan evaporation have been advanced: the first invokes changes in the humidity regime over the pans (*6*), whereas the second invokes reductions in solar irradiance resulting from more clouds and/or aerosols (*5*, *7*) and is generally consistent with the independent suggestion that increased pollution would weaken the hydrological cycle (*8*). The first proposal is that pan evaporation has decreased because evaporation from the environment surrounding the pan has increased (*6*). The explanation is that in water-limited environments, when the evaporation from the adjacent environment is high, the air over the pan tends to be cooler and more humid, thereby reducing evaporation from the pan. A subsequent analysis of rainfall and streamflow data from water-limited environments in both the former Soviet Union and the United States does apparently show an increase in evaporation from the environment (*9*, *10*). However, this explanation for decreasing pan evaporation is unsatisfactory for two reasons. First, it only predicts changes in pan evaporation in water-limited environments. The problem is that some areas are not water-limited, and in wet environments the evaporation from pans and the surrounding environment have both declined (*9*). Further, if the proposed mechanism was the important one, then the vapor pressure deficit should have decreased. However, data from the United States show that its average has remained virtually constant over the past 50 years (*10*). This implies that the second proposal, based on the decrease in solar irradiance, should be further investigated.

Any explanation of the decrease in pan evaporation must accommodate the following: (i) the widespread decrease in pan evaporation has occurred in both dry and wet environments, and (ii) the average vapor pressure deficit ($D$, measured in Pa) has remained more or less constant despite increases in the average temperature. Decreases in solar irradiance would be consistent with (i), and here we specifically address the second item.

The key question is: How could $D$ remain nearly constant despite increases in average temperature? We note that $D$ is defined by

$$D = e_s(T) - e_s(T_d), \qquad (1)$$

where $e_s$ (measured in Pa) denotes the saturation vapor pressure at the temperature ($T$) and dew point ($T_d$) of the air. To first order, the change in $D$ is given by

$$\delta D = s\delta T - s_d \delta T_d, \qquad (2)$$

where $s$ and $s_d$ are the slopes of the saturation vapor pressure–temperature relationship at $T$ and $T_d$, respectively. $T$ is larger than $T_d$, and $s$ is larger than $s_d$. $\delta D$ would be zero if $\delta T_d/\delta T$ were equal to $s/s_d$. Averaged over a day, $s/s_d$ depends on both the average $T$ and the diurnal temperature range (DTR). This ratio is typically a little greater than 2 for a sunny day with a large DTR but a little less than 2 on cloudy days with a lower DTR (Table 1). Taking a typical value of $s/s_d$ as 2 (Table 1), it follows that $\delta D$ would be zero provided that $\delta T_d$ is double $\delta T$. That is important, because globally averaged measurements over the past 50 years show that while the average $T$ has been increasing (~0.15°C decade$^{-1}$), the average minimum $T$ generally has been increasing twice as fast (~0.2°C decade$^{-1}$) as the average maximum $T$ (~0.1°C decade$^{-1}$) (*1*). When above the freezing point, the dew point will in general set a lower limit on the minimum $T$. Thus, the observed increase in minimum $T$ implies that the dew point must also be increasing faster than the average $T$.

**Table 1.** Variation in the ratio $s/s_d$ as a function of $T$ assuming three different $T_d$ ($T_d$ = 5°, 15°, 25°C).

| $T$ (°C) | $s/s_d$ |
|---|---|
| $T_d$ = 5°C $s_d$ = 61 Pa K$^{-1}$ | |
| 10 | 1.36 |
| 15 | 1.80 |
| 20 | 2.38 |
| 25 | 3.10 |
| $T_d$ = 15°C $s_d$ = 110 Pa K$^{-1}$ | |
| 20 | 1.32 |
| 25 | 1.72 |
| 30 | 2.22 |
| 35 | 2.84 |
| $T_d$ = 25°C $s_d$ = 189 Pa K$^{-1}$ | |
| 30 | 1.29 |
| 35 | 1.65 |
| 40 | 2.08 |
| 45 | 2.61 |

Cooperative Research Centre for Greenhouse Accounting, Research School of Biological Sciences, Institute of Advanced Studies, Australian National University, Canberra ACT 0200, Australia.

*To whom correspondence should be sent. E-mail: farquhar@rsbs.anu.edu.au